Available online at www.sciencedirect.com

ScienceDirect

Journal of the European Ceramic Society 26 (2006) 3583–3597

www.elsevier.com/locate/jeurceramsoc

Modification of thermal barrier coating architecture by in situ laser remelting

Guy Antou[a,*], Ghislain Montavon[b,1], Françoise Hlawka[a], Alain Cornet[a], Christian Coddet[b], Frédérique Machi[c]

[a] *LGECO - GLISS, Institut National des Sciences Appliquées de Strasbourg, 24 Bd de la Victoire, 67 084 Strasbourg Cedex, France*
[b] *LERMPS, Université de Technologie de Belfort-Montbéliard, site de Sévenans, 90 010 Belfort Cedex, France*
[c] *IREPA Laser, Pôle API, Parc Technologique, 67 400 Illkirch, France*

Received 9 June 2005; received in revised form 15 December 2005; accepted 6 January 2006
Available online 28 February 2006

Abstract

Yttria partially stabilized zirconia thermal barrier coatings (TBCs) are widely used to protect components of aero gas turbines against high heat fluxes and hence increase their properties by reducing their in-service temperature. However, these coatings degrade in service conditions.

Therefore, manufacturing TBC which present both low thermal conductivity and high life-time is a real challenge. Engineering the coating architecture by an adapted process is a prerequisite to modify TBC characteristics. In this study, laser remelting was combined to thermal spraying in order to modify the TBC properties.

In situ laser treatment (i) changes structure from lamellar to dendritic columnar; (ii) generates a pore architecture less sensitive to sintering, maintaining the TBC thermal and mechanical properties during thermal treatments at high temperatures; (iii) improves the thermal insulation properties of the TBC by decreasing its thermal conductivity of about 30%; (iv) decreases its permeability permitting to reduce oxidation and corrosion phenomena of the underneath layers and substrate; (v) increases the resistance to isothermal shocks (with the possibility to double the number of cycles); (vi) conducts to a metastable tetragonal phase more stable during thermal shocks; (vii) without modifying the elastic response of the deposit.

Keywords: Plasma-laser hybrid process; ZrO_2; Porosity; Thermal properties; Mechanical properties; Coating

1. Introduction

Thermal barrier coatings (TBCs) are widely used in aero- and land-based gas turbines. The benefit of these coatings results from their ability to sustain high thermal gradients in the presence of adequate backside cooling.[1–3] TBC system is hence used to protect the metallic components of the turbine hot parts from degradation at high temperatures, from erosion, from oxidation and corrosion phenomena. To fulfil this global function, four primary constituents compose a thermal insulation system:

(i) The top coat, i.e., the ceramic TBC, which is commonly manufactured using air plasma spray process and behaves as the thermal insulator;
(ii) The substrate materials, most commonly a superalloy, which sustains the structural loads;
(iii) An aluminum containing bond-coat (BC), usually MCrAlY where M represents Ni, Co or a combination of these two elements, located between the metallic substrate and the ceramic, which is usually manufactured using plasma spraying or flame spraying and provides an oxidation protection to the substrate and behaves as a compliance layer due to the linear thermal expansion coefficient mismatch between the ceramic TBC layer and the substrate;

---

[*] Corresponding author at: UMR 6638 SPCTS, ENSCI, 47 – 73 avenue Albert Thomas, 87 065 Limoges, France. Tel.: +33 5 55 45 22 64; fax: +33 5 55 79 09 98.
E-mail address: guy.antou@unilim.fr (G. Antou).

[1] Present address: UMR 6638 SPCTS, ENSCI, 47 – 73 avenue Albert Thomas, 87 065 Limoges, France.

0955-2219/$ – see front matter © 2006 Elsevier Ltd. All rights reserved.
doi:10.1016/j.jeurceramsoc.2006.01.003

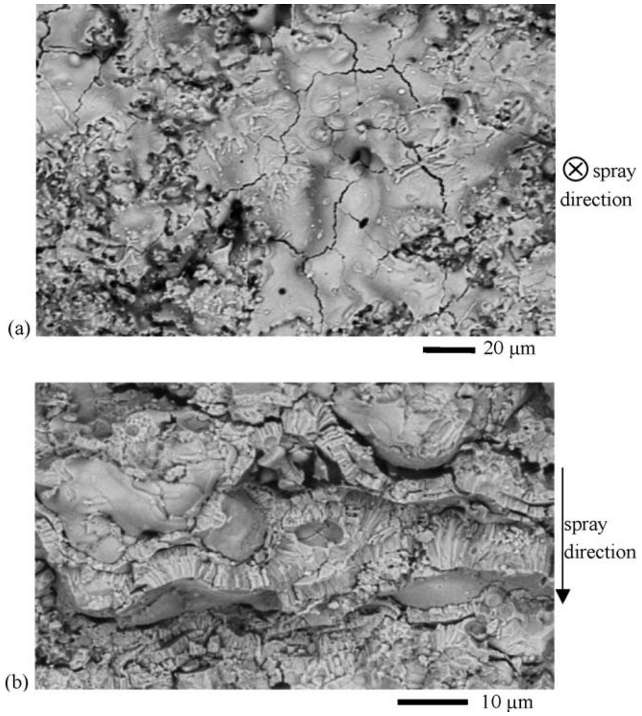

Fig. 1. (a) Thermal sprayed ceramic coating upper surface and (b) internal structure presenting cracks, decohesions and pores constituting an interconnected pore network.

(iv) A thermally grown oxide (TGO), predominantly α-alumina,[4] that grows between the ceramic TBC and the BC during the very first thermal cycles[a] of the system and plays a relevant role in the BC/TBC adhesion.[8,9]

The two main reasons for damage of TBC are: (i) the metal/ceramic thermal linear expansion mismatch during thermal cycling; (ii) the growth of the TGO which induces stresses into the ceramic top coat. These damages induce the failure of the TBC system by spallation of the ceramic top coat.

In the case of thermal spraying, manufactured coatings are characterized by (Fig. 1): (i) cracks and open pores, which increase coating compliance and life-time, but also increase its permeability to the reactive environments (i.e., sulfur, vanadium, etc.); (ii) pores and delaminations, which decrease coating thermal conductivity and increase its compliance, but also increase its permeability. So, the possibility to partially or totally reduce the pore connectivity into as-sprayed coatings appears especially interesting to improve their oxidation/corrosion resistance. Moreover, for advanced gas turbines, improvements of TBC properties are searched out, that is to say: a higher life-time, a lower thermal conductivity, a higher thermal stability and a lower surface roughness. These improvements are searched out to decrease maintenance frequency and to increase efficiency by increasing gas temperatures at the combustion chamber outlet.

To improve TBC characteristics, one way consists in modifying the layer architecture by an adapted manufacturing process. To reach this goal, plasma spraying is combined in this study to laser remelting.

Several studies have been undertaken in the past to modify and especially densify thermal spray coatings implementing laser irradiation.[10–14] Whatever the nature of the coating to treat, the methodology was somehow the same; it consisted in a first step in manufacturing the coating via a classical route and in a second step in post-treating the coating through its overall thickness. In such a case, the resulting microstructures were always made of fine columnar dendrites, but the rapid solidification (i.e., cooling rate ranging between 10^6 and $10^7\ \mathrm{K\,s^{-1}}$)[15] of a large melting pool induced high levels of residual stresses, relaxing via numerous macroscopic cracks and delaminations. Consequently, such microstructures exhibit degraded physical properties, such as degraded gas tightness, fatigue properties and erosion resistance.[15]

In order to modify the structures without generating a too high level of cooling stresses incompatible with mechanical resistance properties, in situ coating remelting appeared as an interesting alternative. This approach, to the author knowledge, was not yet really investigated, except in the works performed in Japan by Ohmori et al.[16,17] The energy source was a Nd: YAG laser. It was shown that the crack formation behaviors of coatings was different from the post-treated coatings, and was characterized as a feather-like structure with a significant number of branching cracks. This microstructure permits to decrease the thermal diffusivity by 60% of the as-sprayed value, whereas post-treated coatings (i.e., which exhibit a thoroughly remelted layer and sharp vertical cracks) showed an increase of approximately 85% of thermal diffusivity compared to the value for as-sprayed coatings. Moreover, the wear property of TBCs can be significantly improved by applying a suitable laser hybrid process.

2. Experimental protocols

2.1. Coating manufacturing and processing parameters

2.1.1. Feedstock materials

Two morphologies of yttria (7 wt.%) partially stabilized zirconia (Y-PSZ) powder were selected as feedstock material: (i) a dense powder, i.e., Plasmatex[b] 108S of particle size distribution ranging from 11 to 33 µm (average 19 µm); (ii) a hollow powder, i.e., Metco[c] 204NS-B of particle size distribution ranging from 28 to 100 µm (average 57 µm). These powders exhibit different particle size distributions. However, no shift was observed as concerns the particle pattern with regard to the plasma torch centerline axis, since the centers of mass of the spray patterns

---

[a] Prior being in service, the TBC system is "stabilized" by heat treatment at high temperature. Among noticeable effects, such as stress relaxation, this treatment permits to develop a first TGO layer at interface. Of course, this layer will further grow in service. The oxygen diffusion, necessarily to the TGO growth, is made possible on the one hand by the permeable character of the ceramic layer (i.e., open pores) and on the other hand by the high ionic conductivity (i.e., $1–10\ \mathrm{S\,m^{-1}}$)[5–7] of Y-PSZ.

[b] Saint Gobain Coating Solutions, Avignon, France.

[c] Sulzer-Metco, Rigackerstrasse 16, 5160 Wohlen, Switzerland.

Table 1
Selected processing parameters[a]

Parameter	Value
Nozzle diameter (mm)	6
Arc current intensity (A)	630
Argon flow rate (SLPM)	44
Hydrogen flow rate (SLPM)	13
Feedstock injector diameter (mm)	1.8
Feedstock injector tip location from gun centerline axis (mm)	6
Feedstock carrier gas flow rate (argon) (SLPM)	3.4
Feedstock mass rate[b] ($g\,min^{-1}$)	15–25
Spray distance (mm)	120
Spray velocity ($m\,min^{-1}$)	30–60
Scanning velocity ($mm\,min^{-1}$)	0.3–0.6

[a] For Sultzer-Metco F4 d.c. plasma torch.

[b] Feedstock mass rate was adjusted according to the spray velocity to keep constant the average deposited thickness per pass. The spray velocity was adjusted to vary the laser energy density. The scanning velocity was adjusted according to the laser energy density to keep constant the laser treated area per spray pass.

at the spray distance in regards to the gun centerline axis were measured to be 7 mm for both powders. Indeed, the particle average trajectories are considered to be identical for the two feedstocks. This indicates almost identical particle momentum density whatever the particle architecture, i.e., dense or hollow. For this reason, no adjustment of the powder injection parameters into the plasma jet was required.

Concerning the bond-coat, a nickel (5 % by weight) aluminum powder was selected. Of course, such a material is not fully representative of standard thermal sprayed bond-coats for TBCs. MCrAlY (where M represents Ni, Co or a combination of these two elements) types bond-coats are more usual. This is why present results cannot be transferred to a realistic TBC system (Y-PSZ, MCrAlY) because Ni–Al bond-coat oxidizes more rapidly. Results rather have to be considered comparatively between as-sprayed and in situ remelted TBCs.

2.1.2. Processing parameters

The experimental device of the hybrid plasma spray process was constituted by the association of a F4 d.c. plasma spray gun of 40 kW from Sulzer-Metco[c] and a laser diode (3 kW, average power) of 848 nm wavelength, from Laserline[d] (Fig. 2). Powders were processed implementing "reference" processing parameters and remelted with several laser energy densities (Table 1). The feedstock mass rate was adjusted consequently with the spray velocity (i.e., the relative velocity between the spray gun and the part to cover), itself depending on the selected laser irradiance, in order to ensure a constant deposited thickness per pass of about 12 μm. The coatings were remelted layer by layer, as they were manufactured, or alternately (i.e., an as-sprayed layer followed by an in situ remelted layer). The input energy effects were studied varying the spray velocity (i.e., from 35 to 60 $m\,min^{-1}$), and consequently the irradiation duration (i.e., from 1.8 to 3.1 ms, respectively). All manufactured coatings were about 220 μm thick.

The interaction between an incident laser beam and a material occurs at the extreme surface where valence electrons of the material and photons of the laser beam interact. Only a fraction of the emitted energy density is absorbed by the material. The absorption coefficient, A, is the ratio of the energy density absorbed by the material to the energy density emitted by the laser. When considering Y-PSZ irradiated by a radiation of 900 nm wavelength, the absorption coefficient is about 0.52.[12] The following results are presented, nevertheless, by considering the laser emitted energy.

2.1.3. Substrates

Two types of substrates were used. Concerning samples for structural attribute quantification, the substrate was cylindrical and made of a low carbon steel (ISO 5235). The motivation for this choice was: (i) to reduce the cost in comparison with superalloys; (ii) to visually check the adhesion of the coating during sample manufacturing (i.e., no spallation) by increasing the stress concentration coefficient at the sample "sharp" edges which leads to an increase of the stresses. Concerning samples for thermal cyclings, the substrate was prismatic (Fig. 3) and made of a stainless steel (AISI 316C). The motivation was: (i) to deal with a substrate with higher mechanical behaviors and higher oxidation/corrosion resistances during thermal shocks; (ii) to reduce coating spallation during thermal shocks by machining large oblique edges.

2.2. Coating structure characterization

2.2.1. Coating structure observation

The samples were cut parallel to the spray direction using a diamond saw in an oil medium, mounted in rings and infiltrated with epoxy (i.e., impregnation technique). They were then polished following standard metallographic techniques (i.e., prepolishing and diamond slurry polishing) on an automatic polishing system. Prior to SEM observation, a carbon layer was deposited by sputtering onto the polished samples.

Besides, some samples were cooled down in liquid nitrogen (i.e., ~77 K) and broken in order to observe the resulting failure facieses.

2.2.2. Phase identification

Phase compositions of as-sprayed and laser treated coatings were investigated implementing a X-ray diffractometer (D500 Siemens, Munich, Germany) (40 kV, 30 mA, Co $K\alpha_1$ radiation at 0.17890 nm). A 2θ scanning step of 0.02° and a measuring time between each step of 6.0 s was used to determinate the peak positions of the different ZrO_2–Y_2O_3 phases in the range of $20° < 2\theta < 110°$. The region of the (0 0 4) and (4 0 0) T′ metastable phase peaks, between 86 and 90°, was especially investigated with a scanning step of 0.01° and a measuring time between each step of 60 s.[18,19]

Besides, the calculation of the yttria content is a way to determine if the coating tetragonal phase is the equilibrium or the metastable tetragonal phase.[18] The calculation of yttria content within the cubic and tetragonal phases was based on the changes

---

[d] Laserline, Maria Trost 23, 56070 Koblenz, Germany.

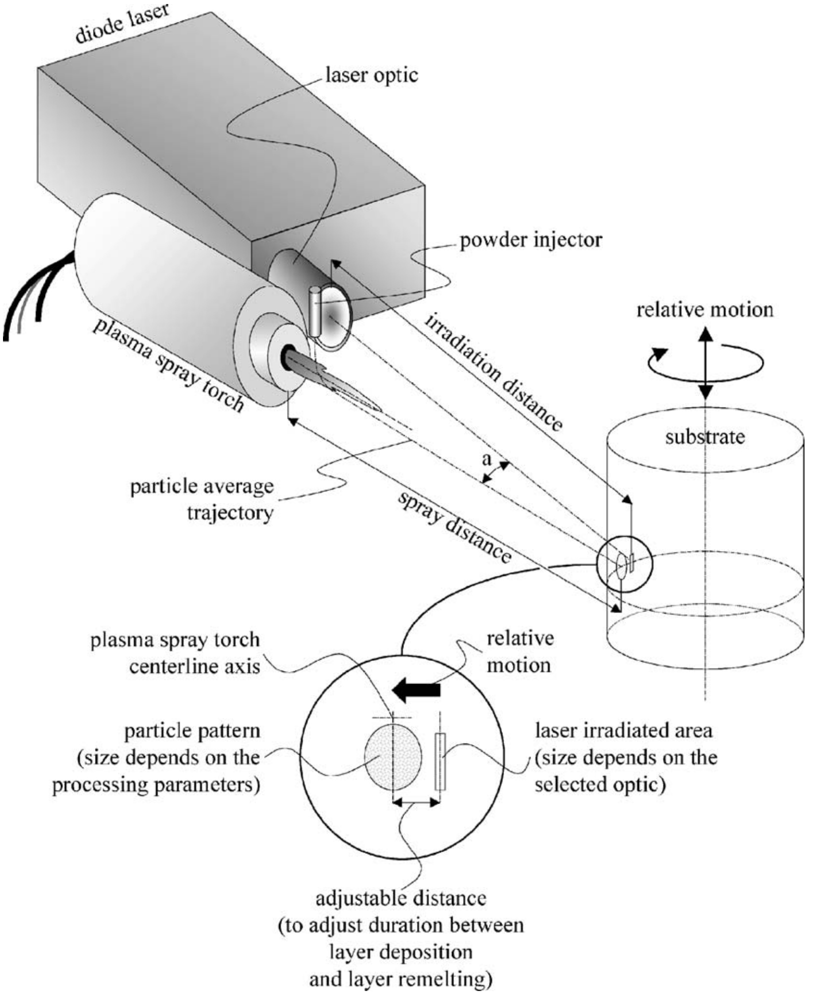

Fig. 2. Experimental device constituted by the association of a plasma spray gun and a diode laser.

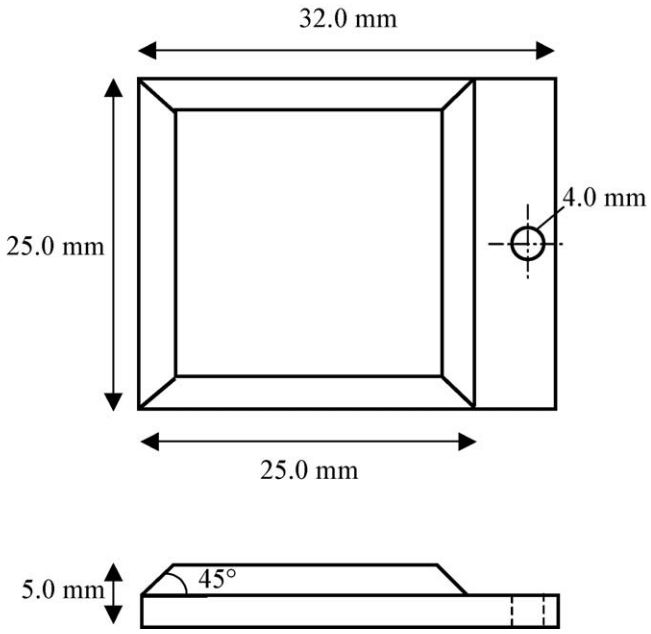

Fig. 3. Substrate shape used for thermal cyclings.

of lattice parameters, as described by Scott[20]:

$$a_t(\text{Å}) = 5.080 + 0.00349X \tag{4}$$

$$c_t(\text{Å}) = 5.195 - 0.00309X \tag{5}$$

where X is the $YO_{1.5}$ content in mol%. The a_t and c_t measurements can be altered by errors in the sample positioning. The c_t/a_t ratio permits, however, to avoid these errors and only takes into account the goniometer accuracy.

2.2.3. Pore-crack network architecture

2.2.3.1. Porosity level quantification. Image analysis was carried out to quantify the overall porosity level and the crack network orientation.[21] SEM images were discretized and analyzed using Image 1.62 software from NIMH (Research Services Branch of the National Institute of Mental Health, Bethesda, MD, USA). Pores and cracks were isolated implementing several filtering and morphological protocols. Pores were then analyzed in terms of numbers and relative surfaces, and cracks in terms of cumulated lengths and orientations. Horizontal and vertical cracks were discriminated and analyzed separately. The cumulated length of cracks per unit surface, L_A (m^{-1}), was calculated for each step of laser energy density in order to deduce the cumulated surface of cracks per unit volume, A_V (m^{-1}), thanks to the following stereological relationship[22]:

$$A_V = \frac{4}{\pi} L_A \quad (1)$$

For each processing parameter set, the results were averaged from 15 fields of view randomly selected across the corresponding polished cross-section.

2.2.3.2. Pore connectivity quantification. Thermal sprayed ceramic coatings, especially Y-PSZ coatings, are characterized by a complex combination of pores and cracks,[9] which form a connected pore network. Pores result mostly from stacking defects when particles impact randomly on the surface, spread and solidify to form lamellae. Cracks result from:

- decohesions between lamellae (i.e., cracks perpendicular to the spray direction, or interlamellar cracks), due to poor surface wettability or to vapors stagnating at the vicinity of the surface where particles impact, among other reasons;
- fractures among lamellae (i.e., cracks parallel to the spray direction, or interlamellar cracks) consecutive to the cooling stress relaxation which developed during solidification and cooling of each individual lamella.

An electrochemical method aiming at qualitatively characterizing the ratio of connected pores was implemented since the measurement of the porosity level via the cross-section observation, for example by image analysis, only permits to characterize the porosity level and not the pore connectivity.

In this test, electrolyte corrodes the substrate more or less, after having impregnated the deposits through their connected pore networks (Fig. 4). In immersion tests, the samples were exposed to a 0.5 mol l^{-1} H_2SO_4 solution at room temperature. A polymer base ring, sealed with a polymer gasket, restricted the surface of contact between the corrosion cell and the coating surface. The apparent area exposed to the electrolyte was 200 mm^2.

The experimental device consisted in a classical three electrodes device, linked to a potentiometer, which measured the current at a fixed potential (420 mV). The electrodes were:

- The working electrode (i.e., the substrate);
- The counter electrode, which measured the current in the circuit;
- The reference electrode (i.e., saturated calomel electrode), leading to the measurement of the potential applied to the working electrode. The reference electrode was immersed in a KNO_3 saturated solution, and was connected to the samples through a salt bridge.

The purpose of these measurements was to measure the evolution of the current density versus time by exposing the coating surface to the electrolyte. As this current is constant for a given electrolyte/metal contact area, the more connected the pores, the higher the measured current. In such a way, the pore connectivity can be estimated qualitatively. The corrosion current is considered as null for non-connected network.

2.3. Coating physical properties

2.3.1. Mechanical properties

2.3.1.1. Berkovich nano-indentation. Hardness (*H*) and effective Young's elastic modulus (*E*) of selected samples were determined using an ultra-low load indentation system equipped with a Berkovich indenter tip (Nano Indenter® XP, MTS Systems Corporation, Eden Prairie, MN, USA). This microprobe records continuously both the load (*P*) and the displacement (*d*) as indents are made on a sample, with resolutions up to 75 mN and 0.04 nm, respectively. Multiple indentations (i.e., about 20) were made on selected samples at different loads in the range of 5–10 mN on coating polished cross-sections. The effective

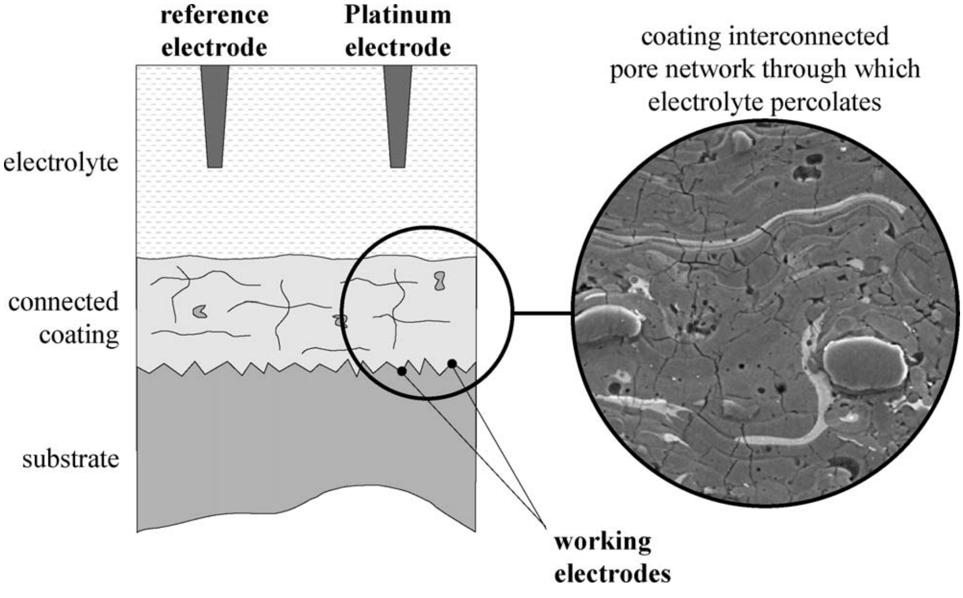

Fig. 4. Experimental device for electrochemical tests.

Young's modulus and the hardness were then calculated from Oliver-Pharr model[23] and the results averaged. The dimensions of the indented zones are several hundred times lower than the lamella average cross-section (i.e., ~1 μm^2 against 750 μm^2, approximately). In such conditions, the Young modulus determination derived from these measurements is related to the intrinsic, or effective modulus, depending on the Y-PSZ structure, exclusively, and not on the coating architectures.

2.3.1.2. Knoop micro-indentation. Selected specimens were indented using a Knoop hardness tester with a 1.962 N test load on the polished cross-sections. Knoop Hardness Values (KHV) were considered as an indicator of the coating cohesion, the higher the KHV, the better the cohesion. The longest diagonal of the indenter was aligned parallel to the coating/substrate interface. The apparent coating Young's modulus was then estimated from Marshall relationship.[24] Fifteen measurements were carried out on each sample and the results were subsequently averaged. The dimensions of the indented zones are about twice the lamella average cross-section (i.e., ~500 μm^2 against 750 μm^2, approximately). In such conditions, the Young modulus determination derived from these measurements is related to the apparent modulus depending on the Y-PSZ structure but also on the coating architectures, that is to say the quality of contact between lamellae.

2.3.1.3. Measurement statistical analyses. Results of nano- and micro-indentation were analyzed implementing Gauss–Laplace and Weibull statistical analyses (Table 2). The estimation of the variability within the hardness distributions was performed by calculating the Weibull parameters,[25] i.e., the Weibull modulus, *m*, and the characteristics value, Xo, which reflect the data scatter and the 63.2 percentile of the cumulative density. The determination of these parameters was done by the curve-fitting method.[26]

2.3.2. Thermal properties

2.3.2.1. Numerical computation of the thermal conductivity. A numerical code was developed and implemented to numerically evaluate the coating thermal conductivity directly from coating SEM views constituting a discrete 2-D domain describing the pore and crack networks.[27] The meshing is directly built from the SEM image: each pixel of the image corresponds to an element. The method consists then in solving the heat conduction equation by the finite volume method in each pixel of the binary image obtained after image analysis. Fig. 5 shows a schematic representation of the solved problem. To each pixel is attributed the thermal conductivity of the corresponding phase: k_m for the solid matrix (3.0 W m^{-1} K^{-1} for Y-PSZ[28]) and k_p for air entrapped in porosity (0.03 W m^{-1} K^{-1})[29]. Results were the temperature value in each pixel of the image and the equivalent thermal conductivity corresponding to the considered field (Fig. 6).

Table 2
Gauss–Laplace and Weibull statistical analyses

Gauss–Laplace	Weibull
Average value	Characteristic value
μ	X_o
50.0% of the cumulative density	63.2% of the cumulative density
Standard deviation	Weibull modulus
σ	m
Probability density function of the distribution	Probability density function of the distribution
$f(x) = \frac{1}{\sigma\sqrt{2\pi}} e^{-(x-\mu)^2/2\sigma^2}$	$f(x) = 1 - e^{(-(x/x_o))^m}$

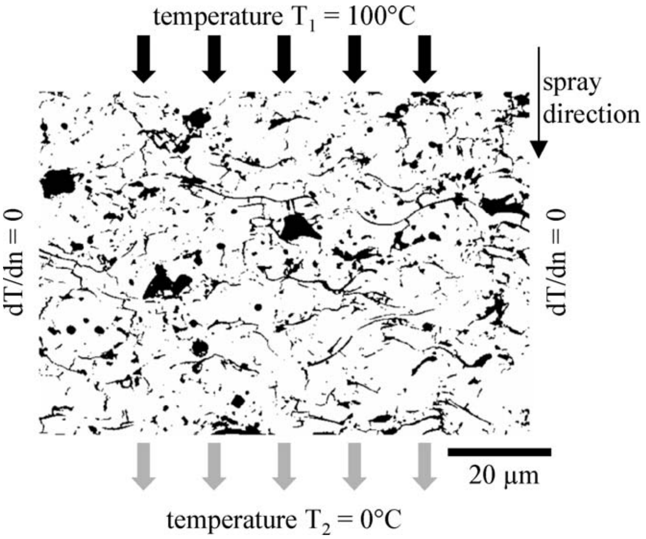

Fig. 5. Problem definition.

Calculation results depend, nevertheless, from the resolution of the coating SEM views, which reproduce more or less faithfully the pore architecture of the coating. Backscattered electron mode was chosen preferentially to secondary electron mode due to the higher contrast between zirconia matrix and porosity (i.e., pores and cracks). Magnification level and image resolution were, respectively, 70 μm × 102 μm and 712 × 484 pixels, inducing a physical resolution of 0.14 μm.

However, this model presents some limits: (i) the image resolution which leads to neglect the peripheral lamellar decohesions (inter-lamellar decohesions lower than 0.1 μm),[30] and hence an overvaluation of the calculated thermal conductivity; (ii) the hypothesis of a constant thermal conductivity for the gas into the pores and the microcracks, whatever their dimensions (i.e., negligence of the Knudsen effect[29]); (iii) the use in calculation of an exclusively two-dimensional method, whereas a three dimensional effect can exist depending on the geometry and on the orientation of cracks and pores. Owing to these various uncertainties, the computation results have to be considered indicative rather than exact. Fifteen calculations were carried out on 15 randomly located images taken on each sample and results were consecutively averaged.

2.3.2.2. Thermal behavior. To compare the thermal behavior of as-sprayed and in situ laser remelted coatings, several thermal treatments were carried out:

(i) *cyclic isothermal shock tests*: the coated specimens were kept in a furnace for 10 min at several test temperatures

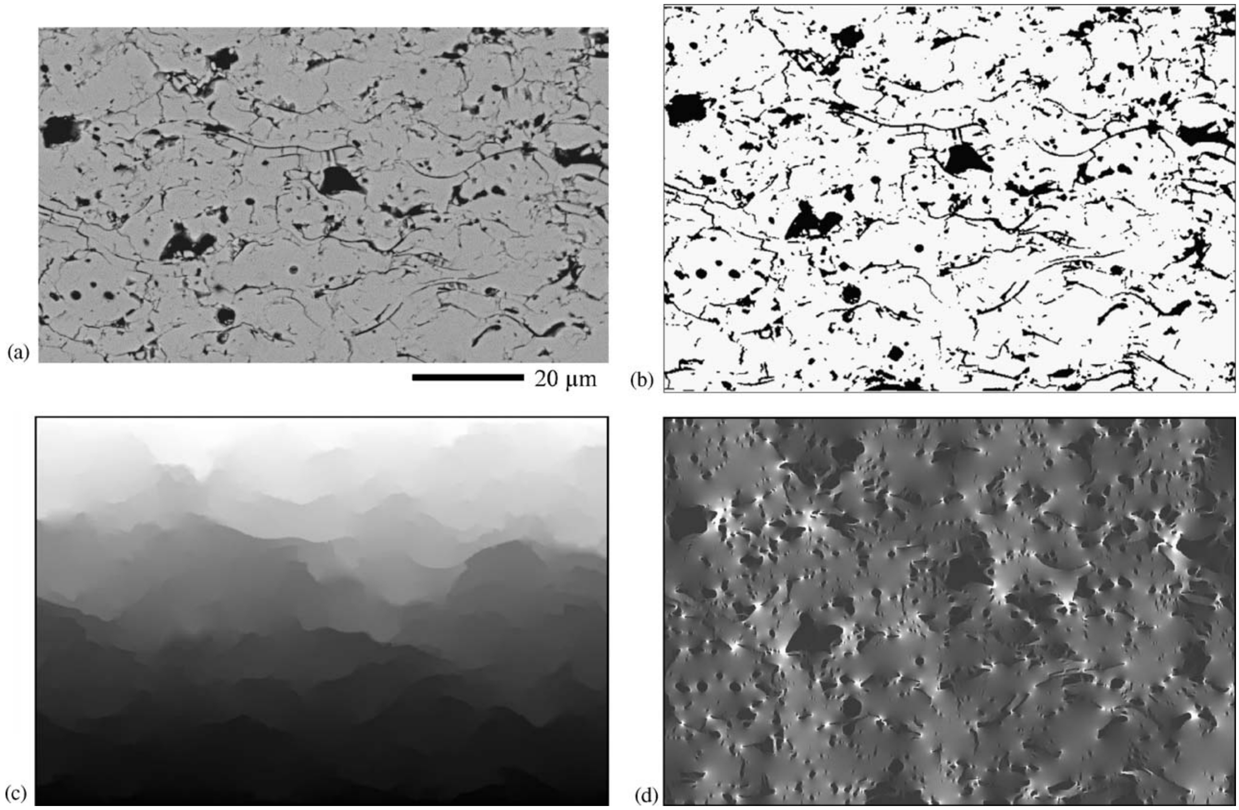

Fig. 6. Methodology of the numerical computations developed to evaluate the thermal conductivity directly from the coating view: (a) SEM cross-section; (b) binary image depicting the pore network; (c) temperature field; and (d) temperature gradient in an as-sprayed YPSZ coating.

ranging from 950 to 1050 °C and then dropped into icy water (0 ± 2 °C). After each thermal cycle, the samples were observed using a stereoscopic binocular. The test was interrupted when the TBC coat surface spalled of from the test zone from more than 50% and the number of cycles recorded. In this test, the average cooling rate was estimated to be about 100 °C s^{-1}. Such a rate is of course not representative of in-service conditions. This severized test was implemented with the unique purpose of comparing, and ranking, the several coating architecture behaviors;

(ii) *cyclic thermal shock tests*: the coated specimens were placed in front of a stoichiometric acetylene flame until its temperature at the back side, measured by a 0.7 mm diameter K type thermocouple inserted in a 1 mm diameter drilled hole and 0.2 mm underneath the coating, reaches 1100 °C (average heating rate of 23 °C s^{-1}) and then cooled by air jet until 50 °C (average cooling rate of 21 °C s^{-1}). After each thermal cycle, the samples were visually observed. The test was interrupted when the coating surface spalled of from the test zone from more than 20% and the number of cycles recorded;

(iii) *thermal annealing* in an air furnace at 1100 °C for 50, 100, 200 and 400 h.

In the present case, Ni–Al bond-coat oxidizes more rapidly than a standard MCrAlY bond-coat. The TGO growth kinetic for Ni–Al is hence higher than for MCrAlY. Consequently, the thermal tests are more severized: a lower number of cycles can be expected for Ni–Al bond-coats in regards to MCrAlY bond-coats. The objective of these thermal tests is to compare as-sprayed and in situ remelted TBCs.

3. Results and analyses

3.1. Coating structure

Whatever the irradiance, the microstructure resulting from laser treatment is a columnar dendritic structure (Fig. 7). The microstructure orientation is typically the one of the directed solidification and indicates the presence of a thermal gradient across the melt fronts generated during laser processing.[31]

Fig. 8 illustrates the interfaces between a non-remelted layer and a remelted layer (Fig. 8a) and between two successive remelted layers (Fig. 8b). The quality of the interfaces is quite good with the continuity of the columnar structure through two successive remelted layers.

3.2. Phase composition

The predominant phase of the coating after in situ laser treatment is the T′ metastable phase (Fig. 9b). The formation of this phase is consistent with the literature, which reports that Y-PSZ coatings containing 8 wt.% Y_2O_3 prepared by plasma spraying or laser treatment produce the metastable tetragonal phase (T′) because of the rapid solidification and subsequent cooling.[32] In addition, the metastable T′ phase is particularly searched out for

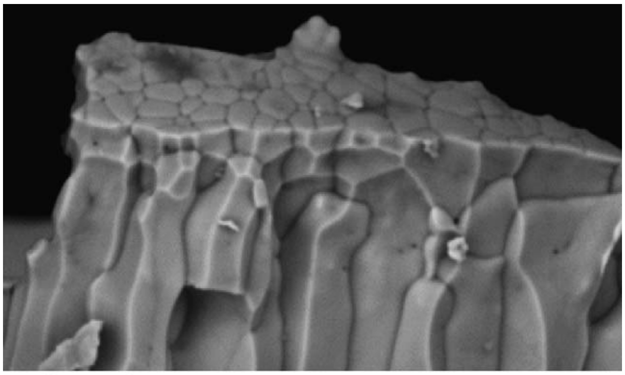

(a) fractography

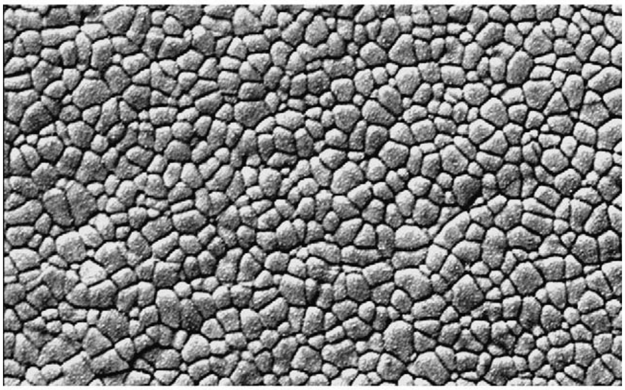

(b) top view

Fig. 7. Columnar dendritic structure of in situ remelted layers.

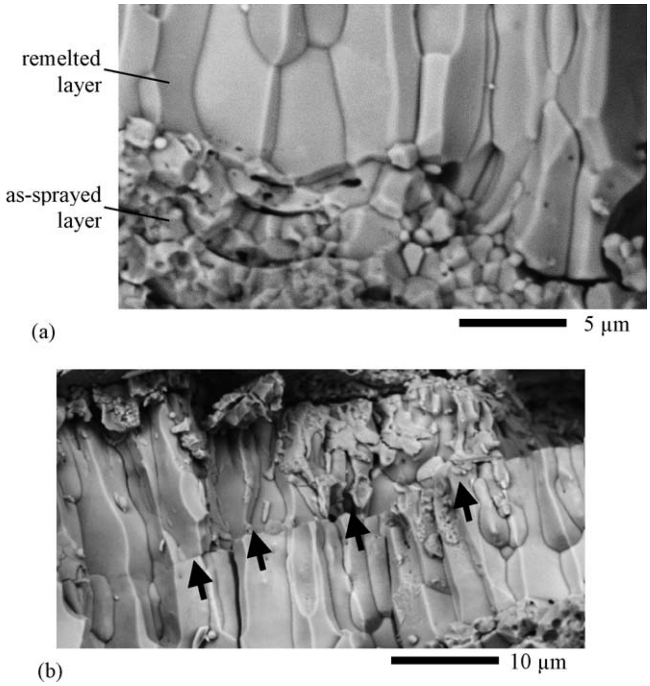

Fig. 8. Interfaces between: (a) a non-remelted layer and a remelted layer; (b) two successive remelted layers.

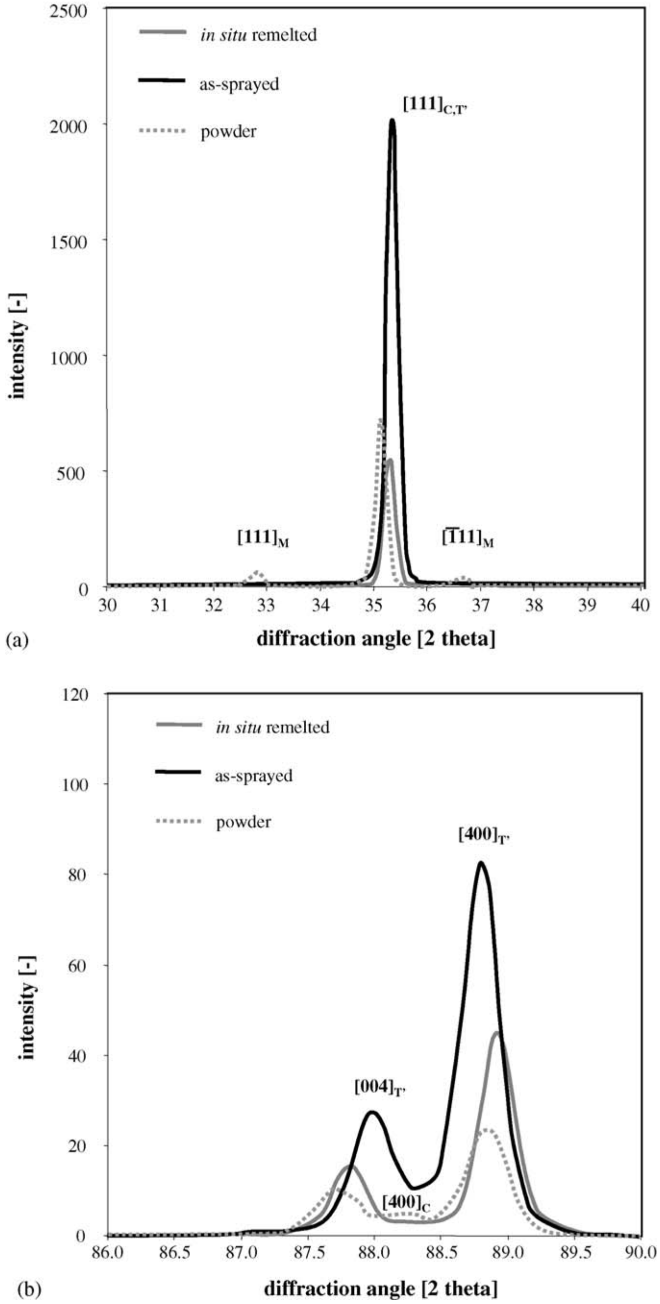

Fig. 9. Typical X-ray diffraction patterns for powders, as-sprayed and in situ remelted coatings: (a) 30–40°; (b) 86–90°.

its tenacity: the exceptional properties of the T′ phase can be explained in terms of structural hardening, i.e., the ability of a grain to release the crack propagation energy.[33]

Besides, the breakdown of the T′ phase into tetragonal (T) and cubic (C) phases was not observed, i.e., the diffusion of the stabilizing elements does not take place during the laser treatment due to the very short duration of exposure at high temperature.

The presence of monoclinic (M) phase, reported to appear near the T′ (1 1 1) region (30–40°) after laser treatment,[19] was not observed whatever the laser processing parameters (Fig. 9a). The phase content of monoclinic is one of the most detrimen-

Table 3
Evaluation of the yttria content for as-sprayed and in situ laser remelted coatings

	Laser energy density (J mm^{-2})	a_t (A)	c_t (A)	c_t/a_t	Y_2O_3	
					(mol%)	(wt.%)
Powders	n.a.	5.11160	5.16412	1.01027	4.8	7.2
As-sprayed	n.a.	5.11384	5.15104	1.00727	5.9	10.7
In situ remelted	2.1	5.10796	5.15752	1.00970	5.0	7.8
	2.5	5.11452	5.16352	1.00958	5.0	7.9

n.a.: non applicable.

tal factors affecting the stability of TBC coatings because the volume expansion accompanied by the T → M phase transformation causes mechanical stresses in the coating.[33]

The results of the evaluation of the yttria content are listed in Table 3. In all cases, the yttria content is higher than 7 wt.%. It is even equal to 10 wt.% for as-sprayed coatings. Since the solubility limit of yttria in the equilibrium tetragonal phase is 4 wt.%, the calculated yttria contents correspond to the presence of metastable tetragonal phase.

3.3. Pore-crack architecture

3.3.1. Porosity level and pore geometric characteristics

Fig. 10 shows typical cross-section morphologies of as-sprayed and in situ remelted TBCs. It appears that the in situ remelting process changes the pore architecture of TBC.

3.3.1.1. Porosity level. Fig. 11 displays the evolution of the coating porosity level as a function of the laser energy density. It clearly shows that the in situ remelting process induces a significant modification of the TBC pore architecture. As a matter of fact, whereas the porosity level related to microcracks is stable, around 4–5%, it clearly appears that the total porosity increases from 8.1% for the as-sprayed coating to about 15% for the remelted coatings. Besides, the total porosity raises from 15 to more than 20% for a laser energy higher than 2.20 J mm^{-2}. This is directly related to an enhancement of the globular porosity level. As a matter of fact, when the laser energy reaches high levels, thermal shocks and remelted thicknesses increase, inducing the formation of large cracks into the deposit. Those cracks are large enough to be assimilated to globular pores.

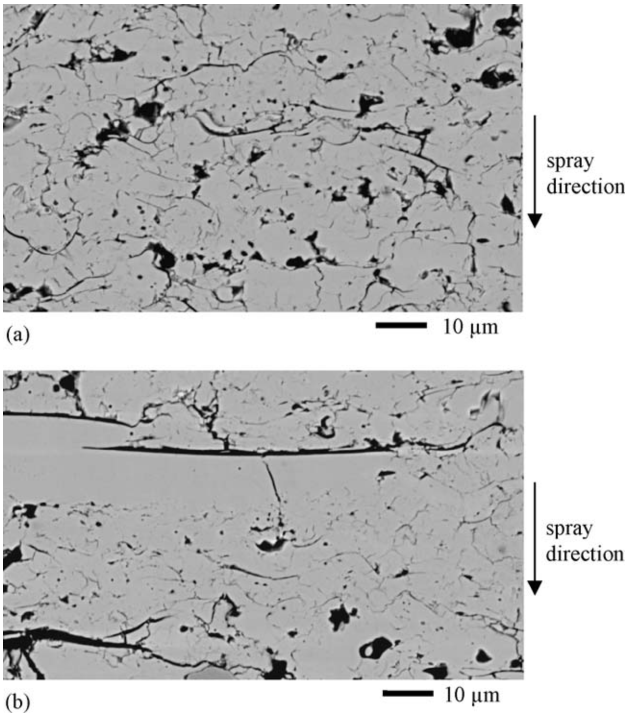

Fig. 10. Typical cross-section morphologies of (a) as-sprayed and (b) in situ remelted TBCs.

3.3.1.2. Crack network orientation. Fig. 12 displays the evolution of the cumulated surface of cracks per unit volume (A_V) for a laser energy density ranging from 1.70 to 2.46 J mm^{-2}. Remelted coatings exhibit a parabolic evolution of the cumulated surface of cracks as a function of the laser energy density. A minimum appears for a laser energy density of 2.07 J mm^{-2}, i.e., a cumulated surface of cracks of 12 mm^{-1} for the horizontal cracks and of 5 mm^{-1} for the vertical cracks. This minimum seems to correspond to a compromise between two phenomena:

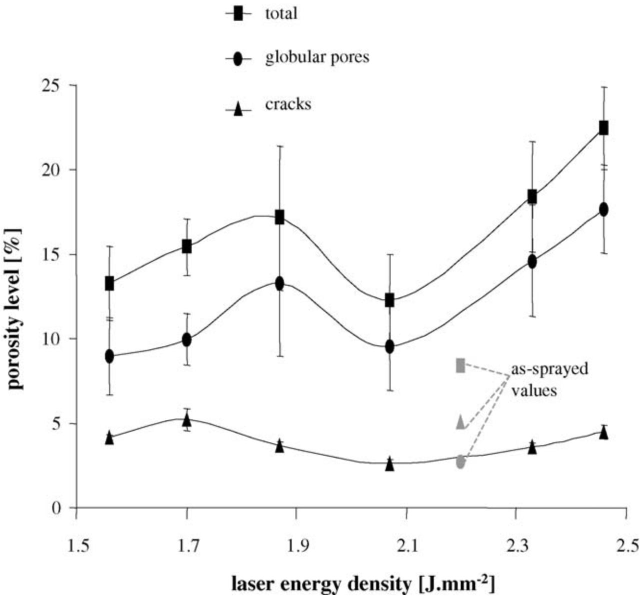

Fig. 11. Evolution of the porosity level as a function of the laser energy density input—dense powder.

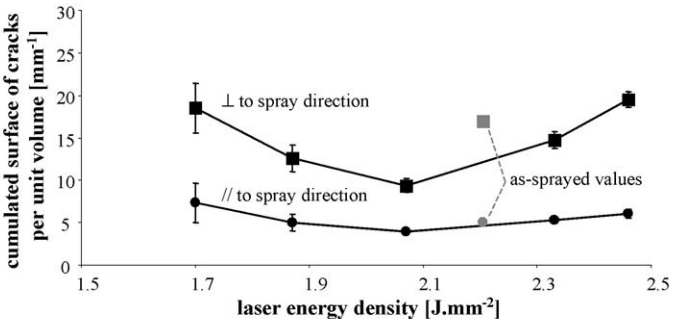

Fig. 12. Evolution of the cumulated surface of cracks per unit volume as function of the laser energy density input—dense powder.

the densification into the remelted areas and the cracks formation due to thermal shocks during laser remelting.

3.3.2. *Pore connectivity quantification*

Fig. 13 displays the evolution of the corrosion current density as a function of the laser energy density. The measurements corresponding to the non-treated samples (i.e., as-sprayed) are specified here for a comparison purpose, taking into account the scanning velocity as the reference parameter. It clearly appears that the current density for in situ laser treated deposits decreases by about 80% compared to the values for as-sprayed deposits, for a laser energy ranging from 1.70 to 1.90 J mm^{-2}. Such an evolution means that the rate of connected pores significantly decreases for this laser irradiation range. This result clearly shows that the gas tightness character of TBCs can be improved by in situ laser remelting. This phenomenon can be observed in Fig. 14: the remelted layer is relatively dense and less cracked than the surrounding as-sprayed layers. This narrow range of laser energy density is related to the fact that: (i) for a laser energy density lower than 1.70 J mm^{-2}, the remelted areas are not large enough to decrease the rate of connected pores; (ii) for a laser energy density higher than 1.90 J mm^{-2}, the remelted layers are larger and consequently more cracked because of the volume reduction during solidification.

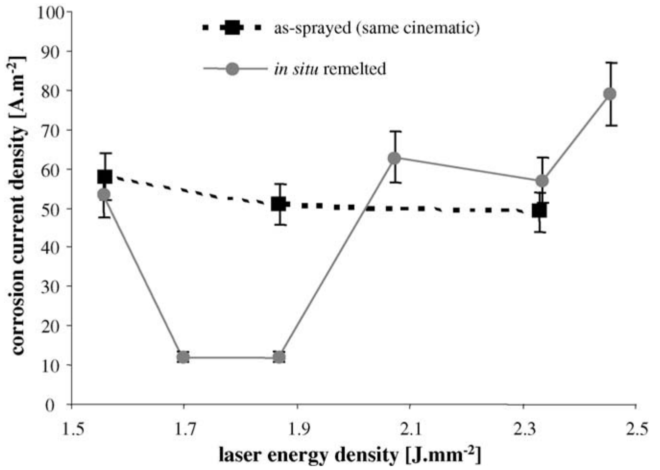

Fig. 13. Results of the electrochemical tests carried out on in situ laser treated samples—dense powder.

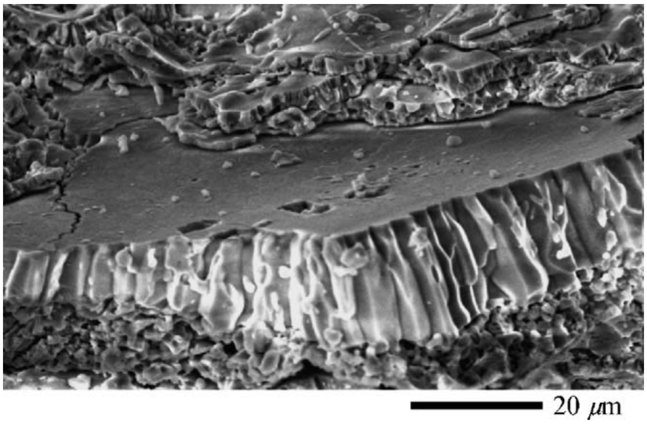

Fig. 14. Dense in situ remelted layer surrounded by as-sprayed layers.

3.4. *Mechanical properties*

3.4.1. *Bulk material (Berkovich nano-indentation)*

Load–displacement (*P*–*d*) curves performed with a 10 mN load for non-treated and laser treated zirconia permit to compare their elastic properties (Table 4). The measured Young's modulus of the as-sprayed Y-PSZ was 259 ± 11 GPa. This value is in accordance with experimental values published in,[18,34,35] which are 206, 237 ± 12 and 250 ± 20 GPa, respectively. A little increase in Young's modulus of about 10% can be noticed after in situ laser treatment. So, in a first approximation, remelted zirconia presents the same elastic properties than non-treated zirconia. This little difference can be related to a little variation of the yttria content between these two types of zirconia. Moreover, a little increase, of about 15%, of the hardness is noticed after laser remelting. Remelted areas with a columnar structure seem to exhibit a slightly enhanced toughness compared to the lamellar structure of the as-sprayed coatings. This could be explained by the fact that fewer columns and their interfaces are indented into remelted zones because the columns of laser treated areas (4–10 μm average diameter) are larger than the columns of non-treated areas (0.5–1 μm average diameter).

Weibull analysis shows that laser treated areas exhibit a higher Weibull modulus of about 30% compared to non-treated areas (Table 5). It means that the large columns of remelted areas are more homogeneous than the small columns of as-sprayed areas.

3.4.1.1. *Coating (Knoop micro-indentation).*

Table 6 shows that KHV increases by about 42%, compared to as-sprayed values, after in situ laser remelting. So, by considering the hardness as a cohesion indicator, such a result means that the

Table 4
Results of the nano-indentation tests (i.e., Berkovich indenter)—hollow powder

	BHV[a] (GPa)	±[b]	E_b[a] (GPa)	±[b]
Laser treated	20.5	1.1	274	13
Non treated	17.4	1.4	259	11

[a] Arithmetic average value from 20 adjusted data points.
[b] Corresponding to half the standard deviation.

Table 5
Weibull analysis performed on results of the nano-indentation test results—hollow powder

	X_o (GPa)	m (−)
Laser treated	21.0	6.3
Non treated	18.9	4.8

Table 6
Results of micro-indentation tests (i.e., Knoop indenter)—hollow powder

Laser energy (J mm^{-2})	KHV[a] (GPa)	±[b]	E_c[a] (GPa)	±[b]
0 (i.e., as-sprayed)	4.4	0.2	21	1
1.67	6.1	0.7	26	3
1.82	5.9	0.8	27	3
2.00	6.3	0.8	28	4
2.22	6.3	1.0	28	4
2.50	5.0	0.8	24	3

[a] Arithmetic average value from 15 adjusted data points.
[b] Corresponding to half the standard deviation.

TBC cohesion is improved by in situ laser remelting. It can be explained by the fact that laser melting effectively removes the voids in the as-sprayed coatings and yields to solid and dense layers, quite similar to a sintered ceramic. Moreover, the coating apparent modulus E_c is kept unchanged in a first approximation after laser treatment, within a 25 GPa order of magnitude.

Weibull analysis allows the characterization of the homogeneity of the results thanks to the Weibull modulus, m. The lower the Weibull modulus, the more scattered the distribution, the more inhomogeneous the related characteristic, the more heterogeneous the coating structure. Fig. 15 displays the evolution of the Weibull modulus, m, of as-sprayed and in situ remelted samples as a function of the laser energy density input. Results show that, whatever the laser energy density, the Weibull modulus of in situ remelted coatings is twice lower than the one of as-sprayed coatings. So, it seems that in situ remelted coatings are more heterogeneous than as-sprayed coatings. It corresponds to the juxtaposition of remelted and non-remelted zones into the in situ remelted coatings. Besides, it appears that the evolution of the Weibull modulus of remelted coatings exhibits two values: (i) for a laser energy density ranged from 1.70 to 2.50 J mm^{-2}, the Weibull modulus of in situ remelted coatings is stable, around 3–4; (ii) for a laser energy density higher than 2.50 J mm^{-2}, the Weibull modulus increases to 5.4. This phenomenon can be explained by the fact that for this latter laser energy density, the remelted zones are larger which induce a more homogeneous remelted coating structure from the macroscopic point of view.

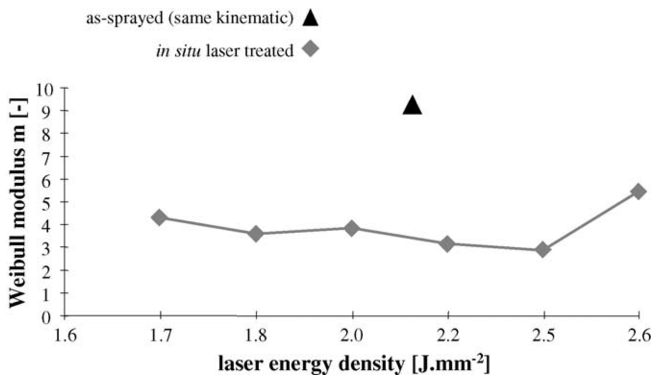

Fig. 15. Evolution of the Weibull modulus, m, of as-sprayed and in situ remelted samples as a function of the laser energy density input—hollow powder.

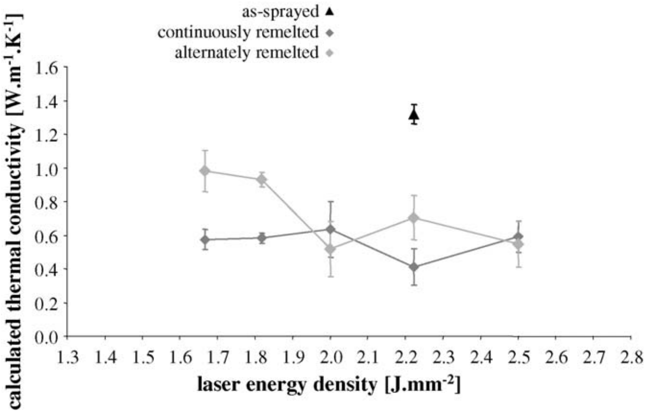

Fig. 16. Evolution of the calculated thermal conductivity as a function of the laser energy density—hollow powder.

3.5. *Thermal properties*

3.5.1. *Thermal conductivity calculation*

The thermal conductivity of each sample was evaluated by numerical computation. The calculated thermal conductivity of as-sprayed coating was 1.4 ± 0.1 W m^{-1} K^{-1}, which is in accordance with the experimental value at 293 K published in[28] (Fig. 16). A decrease of about 30% of the thermal conductivity is obtained for remelted coatings. The thermal conductivity of in situ remelted coating ranges effectively between 0.4 ± 0.1 and 1.0 ± 0.1 W m^{-1} K^{-1}. This evolution seems to be linked to the existence of large horizontal cracks into remelted coating (i.e., as shown by image analysis), which behave as thermal resistances (Fig. 17).

To investigate the coating behavior evolution due to in-service sintering, thermal annealing treatments were carried out. The coating apparent thermal conductivity was then calculated using the 2-D numerical code (Fig. 18). The thermal conductivity of the as-sprayed coating increases from 1.3 W m^{-1} K^{-1} to about 1.7 W m^{-1} K^{-1} for a thermal annealing time of 200 h. It is due to the sintering phenomenon (i.e., the closure of the thinner microcracks by diffusion); it is very emphasized during the first hours of treatment. The thermal conductivity of the in situ remelted coatings also increases, but their higher thermal insulation is maintained; their calculated thermal conductivity is of about 1.2 W m^{-1} K^{-1} for 400 h. It seems thus that remelted structures are less sensitive to sintering thanks to their larger horizontal cracks (Fig. 17).

3.5.2. *Isothermal shocks*

Isothermal shock tests were carried out to investigate the thermal behavior of manufactured coatings.

Evans[2] has shown that the main degradation mechanism during isothermal shocks is due to the growth of the thermally grown

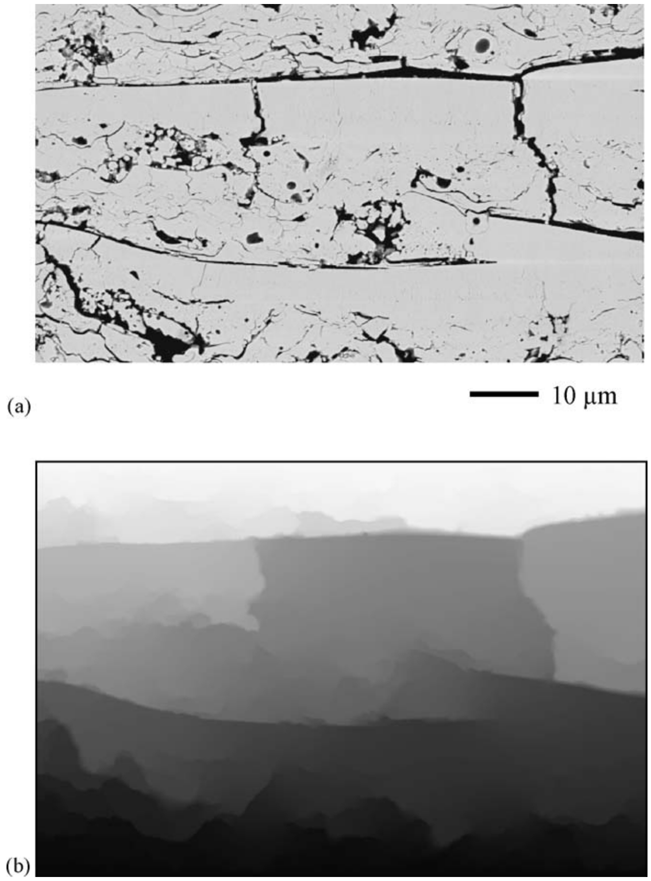

Fig. 17. (a) SEM cross-section and (b) calculated temperature field of an in situ remelted coating (1.56 J mm^{-2}).

oxide (TGO), which induces separations into the coating. These separations propagate then around imperfections induced in the TGO. Finally, they coalesce and become large enough to satisfy large buckling. This is the same observed degradation mechanism in the carried-out experiments (Fig. 19).

Fig. 20 displays the evolution of the number of cyclic isothermal shocks inducing a spallation of 50% of the coated surface for in situ coating remelted with various laser energy densities.

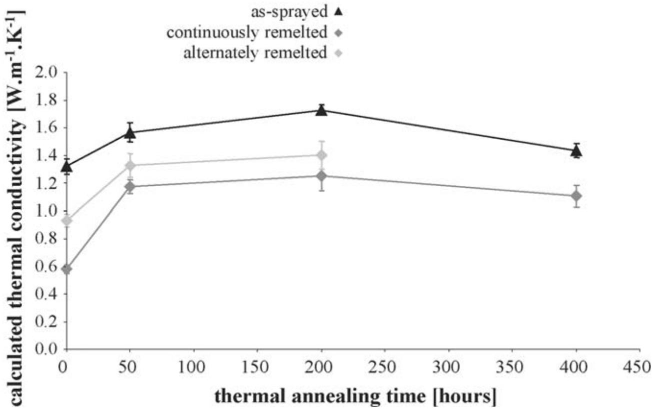

Fig. 18. Evolution of the calculated thermal conductivity as a function of the thermal annealing time—hollow powder.

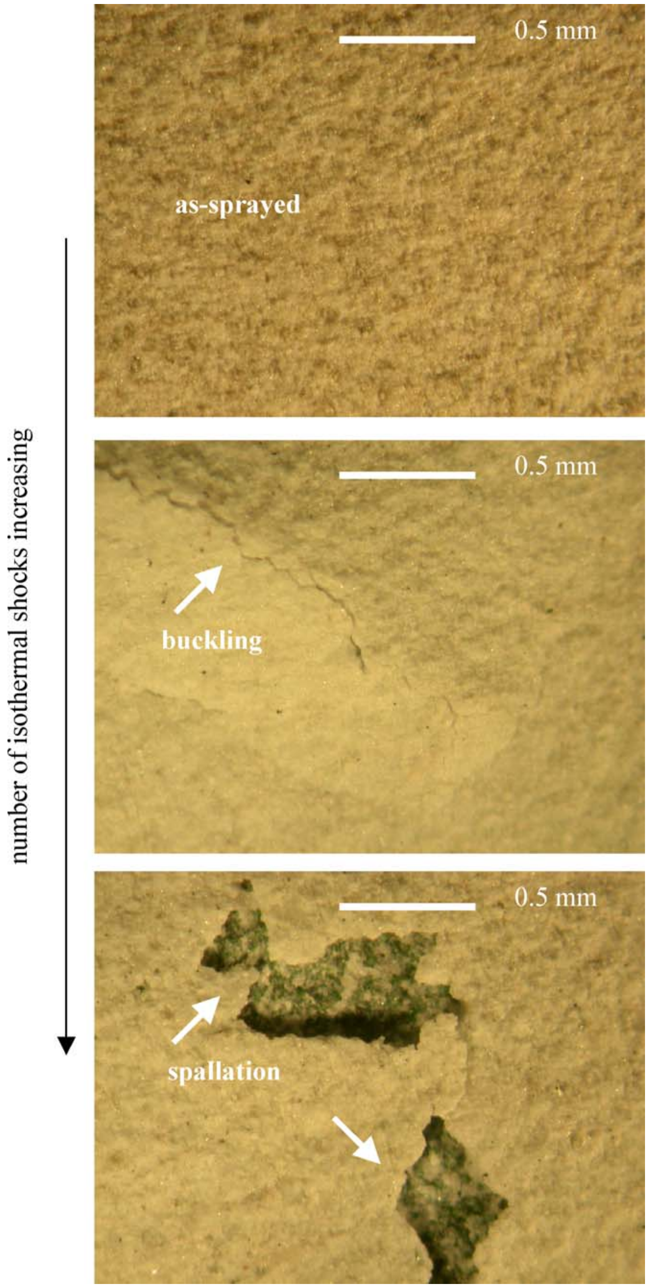

Fig. 19. Observed degradation mechanism during isothermal shocks.

It clearly appears that in situ remelted coatings exhibit better resistance to isothermal shocks than as-sprayed coatings. This resistance is even increased two-fold for samples treated with a laser energy density of 1.70 J mm^{-2}. This indicates that the columnar structure, the pore-crack architecture and the enhanced cohesion (as shown by Knoop micro-indentation) of remelted coatings improve the compliance property and increase the gas tightness of TBCs. This decrease of the connectivity leads certainly to a reduction of the TGO growth kinetic (of course, even if the coating would be completely gas tight, the intrinsic ionic conductivity of zirconia would lead to oxygen diffusion and hence TGO growth. However, the growth kinetic of a TGO which only grows by oxygen diffusion in zirconia superlat-

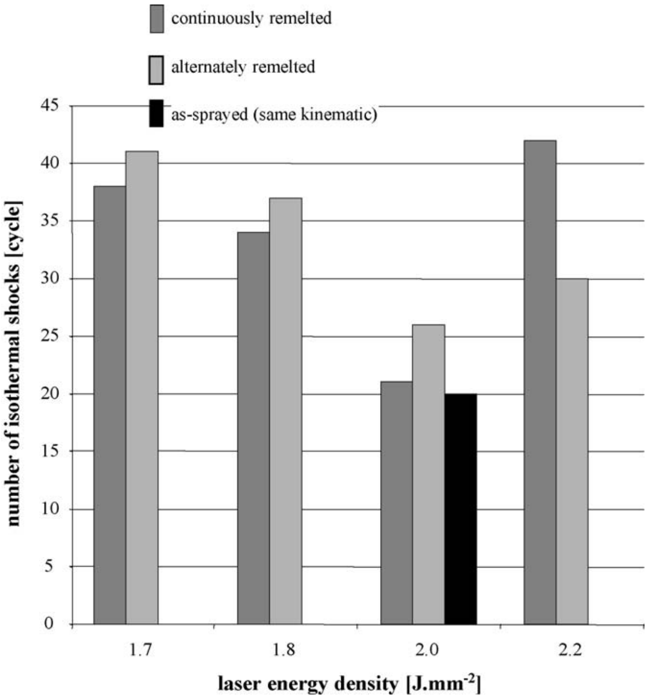

Fig. 20. Isothermal shock resistance at 1273 K for as-sprayed and remelted coatings—hollow powder.

tice would be very likely lower than the growth induced by oxygen diffusion/percolation through the interconnected pore network).

3.5.3. Thermal shock tests

During isothermal shocks, the main degradation mechanism is due to the growth of the TGO. However, for some applications, the degradation mechanism of TBC is more related to the existence of a thermal gradient between the front side and the back side of the coating. So, to study the structures for such a solicitation, thermal shock tests were implemented with a shorter time at high temperature.

As-sprayed and in situ remelted coatings present the same resistance to these shocks, i.e., a resistance of about 75–80 cycles. A too severized test can be one of the reason of these results. However, by identifying the phases inside the thermal shocked coatings, XRD analyses reveal that, even if the metastable tetragonal phase remains the major phase for as-sprayed and remelted coatings after the thermal shock tests, the formation of 21 vol.% of monoclinic phase is detected into as-sprayed coatings (Fig. 21). This result indicates a little come back of the metastable tetragonal phase towards the equilibrium. It means that a part of the metastable tetragonal phase has been converted during the thermal cycle into the equilibrium tetragonal phase. This is accompanied by a yttria diffusion. Then, this equilibrium tetragonal phase transforms into monoclinic phase, which induces the coating failure (because a volume expansion of about 3–5% operates during the transformation $t \rightarrow m$). It seems hence that the in situ laser remelted coatings have higher phase stability during thermo mechanical loads.

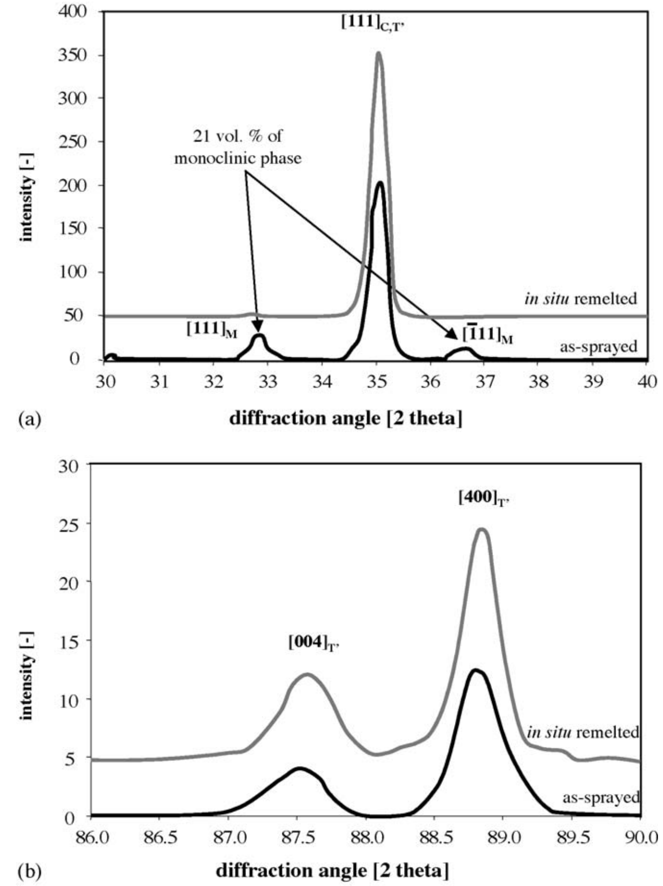

Fig. 21. X-ray diffraction patterns for thermally shocked coatings: (a) 30–40°; (b) 86–90°—hollow powder.

Two hypotheses could explain this:

(i) the pore architecture of the in situ remelted coatings leads to a better compliance in relation to the thermo mechanical stresses, and so to a decrease of the stress variations undergone by the structure during the thermal cycles;
(ii) the residual stress level decreases for in situ remelted coatings. This hypothesis is not directly quantifiable by XRD analyses because the peak shifts due to the yttria content variation are combined to the shifts linked to the residual stresses.

To conclude, it seems that the decrease of the thermo mechanical stresses induced into the TBC structure during the thermal shocks is the main factor which explains the non formation of monoclinic phase into the remelted coatings, and so their best phase stability.

4. Conclusion

The present work was devoted to the modification of Y-PSZ TBC implementing in situ laser remelting with a diode laser. It appears that in situ laser remelting has very emphasized effects on Y-PSZ plasma sprayed structures, which finally improves

TBC properties. As a matter of fact, the association of a high power laser diode to a spray gun permits to:

1. changes structure from lamellar to dendritic columnar;
2. generates a pore architecture less sensitive to sintering, inducing then a best conservation of the thermal and mechanical properties during thermal treatments at high temperatures;
3. improves the thermal insulation properties of the TBC by decreasing its thermal conductivity of about 30%;
4. decreases its permeability in order to diminish oxidation and corrosion phenomena;
5. increases the resistance to isothermal shocks (with the possibility to double the number of cycles);
6. conducts to a metastable tetragonal phase more stable during thermal shocks;
7. without modifying elastic response of the deposit.

Acknowledgements

Authors gratefully acknowledge F. Pandrak, L. Lahoupe from LERMPS-UTBM, and M. Bach from LISS-INSA Strasbourg for their valuable helps. LERMPS is a member of the *Institut des Traitements de Surface de Franche-Comté* (ITSFC, surface treatment institute of Franche-Comté), France.

References

1. Stöver, D. and Funke, C., Directions of the development of thermal barrier coatings in energy applications. *J. Mater. Process. Technol.*, 1999, **92–93**, 195–202.
2. Teixeira, V., Andritschky, M., Gruhn, H., Mallener, W., Buchkremer, H. P. and Stöver, D., Failure of physical vapor deposition/plasma-sprayed thermal barrier coatings during thermal cycling. *J. Thermal Spray Technol.*, 2000, **9**(2), 191–197.
3. Evans, A. G., Mumm, D. R., Hutchinson, J. W., Meier, G. H. and Pettit, F. S., Mechanisms controlling the durability of thermal barrier coatings. *Progress Mater. Sci.*, 2001, **46**, 505–553.
4. Ogawa, K., Masuda, T. and Shoji, T., Kinetic of thermally grown oxide at interface between thermal barrier coatings and MCrAlY bond-coatings. In *Proceedings of Thermal Spray 2001: New Surfaces for a New Millennium*, ed. C. C. Berndt, K. A. Kohr and E. Lugscheider. Pub. ASM International, Materials Park, OH, USA, 2001, pp. 187–194.
5. Stöver, D., Buchkremer, H. P. and Uhlenbruck, S., Processing and properties of the ceramic conductive multilayer device solid oxide fuel cell (SOFC). *Ceramics Int.*, 2004, **30**(7), 1107–1113.
6. Chen, X. J., Khor, K. A., Chan, S. H. and Yu, L. G., Influence of microstructure on the ionic conductivity of yttria-stabilized zirconia electrolyte. *Mater. Sci. Eng. A*, 2002, **335**(1–2), 246–252.
7. Renouard-Valle, G., Elaboration par projection plasma d'électrolytes de zircone yttriée denses et de faible épaisseur pour SOFC. (Elaboration using plasma spraying of Yttria Stabilized Zirconia (YSZ) for SOFCs electrolyte.), Ph.D. thesis, Université de Limoges (Faculté des Sciences et Techniques), France, 2004.
8. Mumm, D. R., Evans, A. G. and Spitsberg, I. T., Characterization of a cyclic displacement instability for a thermally grown oxide in a thermal barrier system. *Acta Materialia*, 2001, **49**, 2329–2340.
9. Rösler, J., Bäker, M. and Volgmann, M., Stress state and failure mechanisms of thermal barrier coatings: role of creep in thermally grown oxide. *Acta Materialia*, 2001, **49**, 3659–3670.
10. Pawlowski, L., Laser treatment of thermally sprayed coatings. In *Proceedings of 2002 International Thermal Spray Conference*, ed. E. Lugscheider. DVS – German Welding Society, Düsseldorf, Germany, 2002, pp. 721–726.
11. Eguchi, N., Zhou, Z., Shirasawa, H. and Ohmori, A., NiCrAlY coatings in YAG laser combined low pressure plasma spraying. In *Proceedings of Thermal Spray: Meeting the Challenges of the 21st Century*, ed. C. Coddet. Pub. ASM International, Materials Park, OH, USA, 1998, pp. 1517–1522.
12. Montavon, G. and Coddet, C., Modification of ceramic thermal spray deposit microstructure implementing laser treatment. In *Proceedings of Thermal Spray 2001: New Surfaces for a New Millennium*, ed. C. C. Berndt, K. A. Kohr and E. Lugscheider. Pub. ASM International, Materials Park, OH, USA, 2001, pp. 1195–1202.
13. Nowotny, St., Scharek, S., Zieris, R., Naumann, T. and Beyer, E., Innovations in laser cladding. In *Proceedings of Laser Materials Processing, Vol 89, ICALEO 2000*, 2000, pp. 11–15.
14. Yuanzheng, Y., Youlan, Z., Zhengyl, L. and Yuzhi, C., Laser remelting of plasma sprayed Al_2O_3 ceramic coatings and subsequent wear resistance. *Mater. Sci. Eng. A*, 2000, **291**, 168–172.
15. Pawlowski, L., Thick laser coatings: a review. *J. Thermal Spray Technol.*, 1999, **8**(2), 279–295.
16. Chwa, S. O. and Ohmori, A., Thermal diffusivity and erosion resistance of ZrO_2–8 wt% Y_2O_3 coatings prepared by a laser hybrid spraying technique. *Thin Solid Films*, 2002, **415**, 160–166.
17. Chwa, S. O. and Ohmori, A., Microstructures of ZrO_2-8 wt% Y_2O_3 coatings prepared by a laser hybrid spraying technique. *Surf. Coatings Technol.*, 2002, **153**(2–3), 304–312.
18. Ibegazene, H., Etude microstructurales de la stabilité thermique de phases métastables dans des systèmes à base de ZrO_2, HfO_2 et d'oxydes de terres rares: application aux barrières thermiques. (Microstructural investigation of thermal stability in ZrO_2, HfO_2 and rare earth sesquioxides based metastable phases: in relation to thermal barrier coatings.), Ph.D. thesis, Université Paris-Sud (U.F.R. d'Orsay), France, 1999.
19. Chwa, S. O. and Ohmori, A., The influence of surface roughness of sprayed zirconia coatings on laser treatment. *Surf. Coatings Technol.*, 2001, **148**, 88–95.
20. Scott, H. G., Phase relationships in the zirconia–yttria system. *J. Mater. Sci.*, 1975, **10**, 1527–1535.
21. Poulain, M., Etude de la conductivité thermique de revêtements céramiques à base de zircone: relation avec la composition, la microstructure et la morphologie. (Thermal conductivity of zirconia based coatings in relation with composition, phases and porous structure.), Ph.D. thesis, Université Paris-Sud (U.F.R. d'Orsay), France, 1999.
22. Underwood, E. E., Stereology, or the quantitative evaluation of microstructures. *J. Microsc.*, 1969, **89**(2), 161–180.
23. Oliver, W. C. and Pharr, G. M., An improved technique for determining hardness and elastic modulus using load and displacement sensing indentation experiments. *J. Mater. Res.*, 1992, **7**(6), 1564–1583.
24. Chiang, S. S., Marshall, D. B. and Evans, A. G., The response of solids to elastic/plastic indentation. *J. Appl. Phys.*, 1982, **53**(1), 298–311.
25. Weibull, W., A statistical distribution function of a wide applicability. *J. Appl. Mech.*, 1951, **18**, 293–297.
26. Devore, L., *Probability and Statistics for Engineering and the Sciences* (*3rd ed.*). Pub. Brooks-Cole Publishing Company, Pacific Grove, CA, USA, 1991, 542 p.
27. Antou, G., Bolot, R., Montavon, G., Coddet, C., Hlawka, F. and Cornet, A., Prediction of thermal spray coating thermal conductivity by 2D heat transfer modelling. In *Proceedings of 2004 International Thermal Spray Conference*, May 2004.
28. Dutton, R., Wheeler, R., Ravichandran, K. S. and An, K., Effect of heat treatment on the thermal conductivity of plasma-sprayed thermal barrier coatings. *J. Thermal Spray Technol.*, 2000, **9**(2), 204–209.
29. Litovsky, E., Shapiro, M. and Shavit, A., Gas pressure and temperature dependences of thermal conductivity of porous ceramics materials. part I. Refractories and ceramics with porosity below 30%. *J. Am. Ceramic Soc.*, 1992, **75**(12), 3425–3439.
30. Bianchi, L., Lucchese, P., Denoirjean, A. and Fauchais, P., Microstructural investigation of plasma sprayed alumina splats. In *Proceedings of Thermal Spray Science and Technology (NTSC95)*, ed. C. C. Berndt. Pub. ASM International, Materials Park, OH, USA, 1995, pp. 255–260.

31. Gaümann, M., Gilgien, P. and Kurz, W., (in French) “La solidification des métaux traités par laser” (On the solidification of metals treated by laser). *CLP Bulletin de Liaison*, 2000, **34**, 9–24.
32. Siegel, R. and Howell, J. R., *Thermal Radiation Heat Transfer* (*4th ed.*). Pub. Taylor and Francis, New York, NY, USA, 2001, p. 112.
33. Lelait, L., Etude microstructurale fine de revêtements céramiques du type barrière thermique: incidence sur la résistance thermomécanique de ces revêtements. (Microstructural study of thermal barrier coating application of the thermomechanical resistance of this coating.), Ph.D. thesis, Université Paris-Sud (U.F.R. d’Orsay), France, 1991.
34. Jang, B.-K. and Matsubara, H., Influence of porosity on hardness and Young’s modulus of nanoporous EB-PVD TBCs by nanoindentation. *Mater. Lett.*, 2005, **59**, 3462–3466.
35. Kurosaki, K., Setoyama, D., Matsunaga, J. and Yamanaka, S., Nanoindentation tests for TiO_2, MgO, and YSZ single crystals. *J. Alloys Compd.*, 2005, **386**, 261–264.